AIAA SciTech Forum
January 3-7, 2022, San Diego, CA & Virtual
AIAA SCITECH 2022 Forum
10.2514/6.2022-1561

Experimental Characterization of Wave-Induced Azimuthal Ion Velocities in a Hollow Cathode Plume

Parker J. Roberts *and Benjamin A. Jorns †
University of Michigan, Ann Arbor, Michigan 48109

Vernon H. Chaplin ‡
Jet Propulsion Laboratory, California Institute of Technology, Pasadena, California 91109

The impact of low-frequency, gradient-driven plasma waves on ion velocities in a magnetized hollow cathode plume is assessed experimentally. Oscillations in the ion velocity distribution are observed directly with time-resolved laser-induced fluorescence velocimetry. 1D quasilinear theory is used to predict the time-averaged drift and energy spread imparted to the ion population by these waves. Ion heating effects are discussed, and both the observed ion distribution and its velocity moments are related to theoretical values. It is found that the ion velocity distribution exhibits strong oscillations in the azimuthal direction, as well as a time-averaged swirl drift of 1-2 km/s and increased azimuthal temperatures of up to 8-10 eV. Wave-induced acceleration is able to account for the magnitude of bulk acceleration experienced by the ions, as well as the characteristics of the perturbation to the distribution function. Measured ion temperatures exceed the predictions from quasilinear heating, but are spatially correlated with the amplitude of the wave oscillation.

I. Introduction

As Hall thrusters, a type of E×B plasma accelerator, are increasingly baselined as propulsion systems for long duration missions in deep space, accurate assessments of thruster lifetime are becoming crucial. This has driven a need to understand and mitigate the principal mechanism of lifetime limitation in these devices: the erosion of plasma-wetted surfaces through sputtering by energetic ions [1]. Historically, the dominant source of this erosion has been the sputtering of the discharge channel walls [2]. Recent innovations based on modifying the magnetic field topography (termed "magnetic shielding") have been shown to virtually eliminate this channel erosion, thereby increasing thruster lifetime by a factor of ten [3, 4]. In its place, however, slower sources of erosion have emerged as potential major lifetime limitations. Most notably, wear tests of shielded thrusters have demonstrated sputtering of the front pole and cathode keeper surfaces [5, 6]. While these erosion processes are far slower than the previously rapid rate of channel erosion, they still pose a risk to long-term thruster health over mission profiles lasting several tens of thousands of hours [7].

This potential risk has led to a number of efforts to characterize and predict the pole erosion process. Simulations and experiments revealed that the anomalous pole erosion on the 6-kW H6MS thruster, the device on which this phenomenon was originally observed, could be explained by an increased flux of divergent ions due to the downstream shift of the acceleration region in magnetically shielded thrusters [8]. However, in the Advanced Electric Propulsion System (AEPS) Hall thruster, plasma simulations have shown that classical, steady-state mechanisms, such as electrostatic acceleration, ionization, and charge exchange, are insufficient to resolve the observed erosion under some conditions [9]. The existence of low-frequency global discharge current oscillations can account for the majority of the erosion at higher-voltage operating conditions where these oscillations are large. Simulations demonstrate that an axially shifting acceleration region leads to increased beam divergence during some phases of the oscillation, which allows for ion trajectories which impact the pole cover [10]. As for the erosion observed at other operating conditions without strong axial oscillations, experiments and simulations have implicated large ion temperatures in excess of 10 eV near the poles as a direct contributor to the large erosion rates seen there. Measurements of the ion velocity distribution function (IVDF) normal to the pole surface of magnetically shielded Hall thrusters have observed a range of axial kinetic energies [11, 12]. Taking this distribution breadth into account yielded closer predictions to measured erosion

*Ph.D. Candidate, Department of Aerospace Engineering, 1919 Green Rd Rm B107, Student Member AIAA
†Assistant Professor, Department of Aerospace Engineering, Associate Fellow AIAA.
‡Technologist, Electric Propulsion Group, Member AIAA

rates than calculations based on monoenergetic ions. With that said, while it appears that the presence of these "hot" ions may explain the erosion, the mechanism driving this increase in ion temperature remains unknown.

To address this open question, it has been suggested that local plasma instabilities in the near pole region may lead to effective ion heating. Mikellides and Lopez Ortega, for example, proposed that lower-hybrid waves with frequencies on the order of 1 MHz heat ions near the pole surface [13]. These instabilities may form due to counterstreaming beam and cathode ion populations across electrons confined in a perpendicular magnetic field [14]. Because this type of instability is not strongly Landau damped by ions, the waves can cause kinetic ion heating as they grow. Simulations incorporated an approximate model for this anomalous ion heating by scaling the ion temperature with the growth rate of the modified two-stream instability (MTSI), a type of lower-hybrid instability (LHI). These modified models predicted erosion at a variety of thruster operating conditions with increased accuracy [15]. While the contribution of lower-hybrid waves has proven to be a promising theory for increased pole erosion rates, lower-hybrid instabilities have not yet been experimentally observed in a Hall thruster plasma.

Another possible contributor to ion energization in the near field is the presence of rotational electrostatic waves in magnetized cathode plumes. These lower-frequency modes (50-100 kHz) were first observed experimentally to propagate primarily in the azimuthal direction via high-speed imagery in Hall thrusters [16] and subsequently have been found in a number of thrusters and configurations [17–19]. Time-resolved Langmuir probe measurements in the 9-kW H9 Hall thruster revealed a localized region of large azimuthal wave amplitudes off-axis near the cathode exit [17]. These waves are large amplitude (~100% oscillations in background density) and are associated with an anti-drift fluid wave driven by the strong radial density gradient in the cathode plume. The anti-drift modes have also been shown to influence anomalous electron cross-field transport in the plume region [17, 20]. As with the LHI, however, these large-amplitude rotational waves observed in Hall thruster cathode plumes may exchange energy with the ion population, leading to a bulk ion drift and increased variance in kinetic energies.

By accelerating or heating the ions near plasma-wetted surfaces, these waves could provide a mechanism for increased ion energy flux, leading to elevated erosion rates at the pole and cathode keeper compared to classical predictions. This hypothesis is consistent with evidence of a rotational bias found by masking erosion of the cathode keeper in recent wear tests [6]. However, while the dispersion and amplitudes of these waves have been examined extensively, their impact on the ion energetics has yet to be characterized. In light of their potential role in pole erosion, there is thus a compelling need to investigate the impact of azimuthal cathode waves on ion energies near the cathode keeper and inner pole of a Hall thruster.

To address this problem, our goal in this paper is to characterize experimentally the correlation between the time-resolved ion properties and azimuthal modes in a magnetized hollow cathode discharge. This paper is organized as follows: Section II discusses the mechanism by which anti-drift waves in the cathode plume may accelerate and heat ions. Section III contains a description of the experimental apparatus used to obtain non-invasive, time-resolved measurements of the azimuthal ion distribution in a hollow cathode plume, as well as a brief description of the analysis techniques applied to this data. Section IV presents the results of these experiments, while Section V discusses the relationships between the experimental results and predictions of ion acceleration and heating. Finally, section VI provides a summary of key conclusions.

II. Theory

In this section, we begin with a general description of the anti-drift waves found in Hall thruster hollow cathodes. We then apply quasilinear theory to demonstrate the mechanism by which these cathode waves can affect the azimuthal ion velocity distribution.

A. Overview of anti-drift waves

The hollow cathode of a Hall thruster acts as the electron source for the discharge. Compared to the rest of the Hall thruster plasma, the cathode plume is relatively dense. The resulting radial pressure gradient gives rise to a diamagnetic drift which can fuel plasma instabilities. Below, we follow Refs. 16, 21, 22, and 17 in the use of a multi-fluid formulation to demonstrate the dispersion of one such instability: the gradient-driven anti-drift wave.

We model the near-field cathode plume as a cylindrical plasma column with axial magnetic field ($\vec{B} = B_0\hat{z}$) and an electric field and density gradient which point inward radially ($\vec{E}_0 = -E_0\hat{r}$, $\frac{dn_0}{dr} < 0$). We assume isothermal electron temperature, so that the pressure force may be written as $-\nabla p_e = -eT_e\nabla n_0$, where T_e is the electron temperature in eV. This coordinate system convention is shown in Fig. 1. Solving the electron momentum equation perpendicular to $\vec{B}$

with inertia and collisions neglected for these conditions leads to the azimuthal electron drift velocity

$$\vec{u}_{e0\perp} = \left[-\frac{T_e}{nB_0}\frac{dn_0}{dr} + \frac{E_0}{B_0} \right] \hat{\theta}, \tag{1}$$

where e is the fundamental charge, and $\hat{\theta}$ is the unit vector in the azimuthal direction. This drift is in the azimuthal direction, and is a combined effect of the $E \times B$ and diamagnetic gradient drifts.

Ions are unmagnetized due to their large mass, and we assume quasineutrality ($n_i \approx n_e$) due to the low frequency of the waves ($\omega << \omega_{ce} < \omega_{pe}$). We allow electrons and ions to stream along the field lines with speeds u_{e0z} and u_{i0z}, respectively. While the waves in question are cylindrical in nature and require a global model based on cylindrical coordinates for full description [16], it is useful to apply a locally Cartesian approximation to compare with point measurements, with the substitution $x \rightarrow r\theta$. We assume cold, collisionless ions but invoke the electron-neutral collision frequency along field lines $\nu_e < \omega_{ce}$. We then linearize the two-fluid equations as in Ref. 17 with assumed axial-azimuthal dispersion $n_1 = \Re\left[\tilde{n}_1 \exp\left[i\left(m\theta + k_z z - \omega t\right)\right]\right]$, where $\tilde{n}_1$ is the complex amplitude, and $\Re$ denotes the real part. This results in the algebraic dispersion relation

$$0 = -\frac{1}{K} + \frac{eT_e}{m_i}\left(\frac{k^2}{(\omega - \vec{k}\cdot\vec{u}_i)^2}\right). \tag{2}$$

In Eq. 2, the proportionality constant K is a complex function of the local plasma properties given by

$$K = \frac{\omega - \frac{m}{r}v_{ExB} - k_z u_{ez} + i\nu_{pl}}{\frac{m}{r}v^* + i\nu_{pl}}, \tag{3}$$

where $m \sim k_\theta r$ is the azimuthal mode number, r is the radial coordinate, and v_{ExB} and v^* are the Hall and diamagnetic drift speeds, respectively. The collisional term $\nu_{pl} = k_z^2 T_e/(m_e \nu_e)$ mediates the phase delay between n_1, $\vec{u}_{i1}$, and ϕ_1. This framework results in a potential fluctuation $\phi_1 = \Re\left[\tilde{\phi}_1 \exp\left[i(\vec{k}\cdot\vec{r} - \omega t)\right]\right]$ which is proportional to the density perturbation n_1 to linear order, via the relation

$$\tilde{\phi}_1 \approx KT_e\left(\frac{\tilde{n}_1}{n_0}\right). \tag{4}$$

Substituting these relationships into the linearized ion momentum equation yields the corresponding azimuthal velocity amplitude

$$\tilde{u}_{i1\theta} = \frac{e\tilde{\phi}_1}{m_i}\frac{m}{r}\frac{1}{\omega - k_z u_{i0z}}, \tag{5}$$

which represents the magnitude and phase of the perturbed ion velocity due to the wave acceleration. Below, we apply these relationships to predict the expected ion velocity and temperature vary as a result of the wave behavior.

B. Impact of anti-drift waves on ion energy distribution function

We now turn to kinetic theory to elucidate how these oscillations can act back on the ion velocity distribution, beginning with the first-order response. Consider the 1D Vlasov equation for unmagnetized ions in the azimuthal direction ($x = r\theta$), assuming an approximately Cartesian formulation:

$$\frac{\partial f_i}{\partial t} + v_x\frac{\partial f_i}{\partial x} + \frac{eE_1}{m_i}\frac{\partial f_i}{\partial v_\theta} = 0. \tag{6}$$

Here, we only consider the contribution of the perturbed electric field in the azimuthal direction, i.e. $\vec{E}_1 \approx E_1\hat{\theta}$. We invoke a first-order perturbation analysis to write the distribution as

$$f_i = f_0 + f_1, \tag{7}$$

where we assume that the waves are electrostatic and that the azimuthal field E_1 is entirely due to the perturbation. We then use an Eikonal approximation to express the perturbed quantities as $f_1 \sim e^{i(kx-\omega t)}$, and invoke method of characteristics to solve for f_1, yielding

$$f_1 = \frac{eE_1}{2m_i}\frac{\partial f_0}{\partial v_\theta}\left[\frac{1}{i(\omega - kv_\theta)}\right]e^{i(kx-\omega t)} + C.C., \tag{8}$$

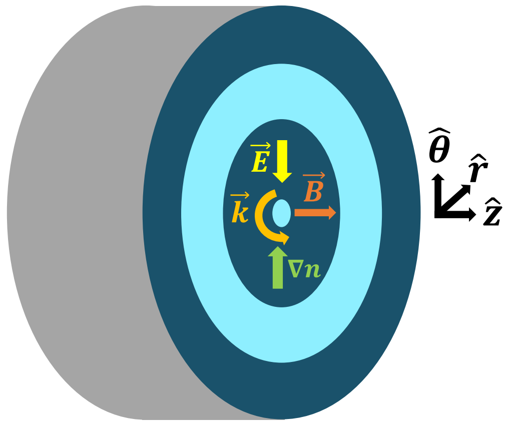

Fig. 1 Illustration of the cylindrical coordinate system used near the cathode plume of a Hall thruster, demonstrating the direction of the electric and magnetic fields, the density gradient, and the wave vector.

where C.C. denotes the complex conjugate. The singularity in Eq. 8 is avoided by allowing for a complex-valued frequency $\omega = \omega_r + i\gamma$, where γ is the growth rate and ω_r is the real component of the frequency:

$$f_1 = \frac{eE_1}{2m_i}\frac{\partial f_0}{\partial v_\theta}\left[\frac{-\gamma}{(\omega_r - kv_\theta)^2 + \gamma^2} - \frac{i(\omega_r - kv_\theta)}{(\omega_r - kv_\theta)^2 + \gamma^2}\right]e^{i(kx-\omega t)} + C.C. \tag{9}$$

The relationship between frequency, growth rate, and wavenumber can be inferred from the anti-drift wave dispersion relation (Eq. 2). Thus, for a given wave frequency, in principle, we can find the time-varying component of the distribution function. If we assume a Maxwellian distribution for the background distribution (f_0), we see from Eqs. 7 and 9 that the time-resolved component will scale with the derivative of this. The derivative is an odd function, which implies that the total distribution will appear to shift back and forth with respect to the mean velocity of the background distribution on the time-scale of the waves.

The above formulation highlights the time-resolved response of the distribution function to the drift wave, but it does not indicate how the time-averaged, background distribution, f_0 is impacted by the oscillating waves. We do expect, however, that the waves might be able to add both momentum and energy to the background population. To motivate a theoretical framework for this, we consider the 3D Vlasov equation for f_0, averaged over a time period greater than the wave period. We find that

$$\frac{\partial f_0}{\partial t} + \vec{v}\cdot\nabla f_0 + \frac{e}{m_i}\vec{E}_0\cdot\frac{\partial f_0}{\partial \vec{v}} = -\left\langle \frac{e}{m_i}\vec{E}_1\cdot\frac{\partial f_1}{\partial \vec{v}}\right\rangle, \tag{10}$$

where $\langle..\rangle$ denotes the average over the phase of the propagating waves. The term on the RHS represents an effective collision term quantifying the action of the oscillating electric field back on the time-averaged ion distribution to quasilinear order. We can use Eq. 10 as the master equation for deriving successive moments of the background distribution function, including the density $n_0 = \int f_0 d^3v$, the drift velocity $\vec{u}_{i0} = \int \vec{v} f_0 d^3v/n_0$, and the ion temperature (in units of eV) $T_i = m_i/(3en_0)\int(\vec{v}-\vec{u}_{i0})^2 f_0 d^3v/n_0$. These properties provide a velocity-averaged indication of the relative drift and energy variance coupled to the background distribution from the quasilinear wave behavior.

With this in mind, we $f_0(\vec{v})$ is isotropic and take the first moment of the governing equation to find the ion momentum equation to find

$$m_i n_0 \frac{\partial \vec{u}_{i0}}{\partial t} + m_i n_0 (u_{i0}\cdot\nabla)\vec{u}_{i0} = en_0\vec{E}_0 + e\nabla(n_0 T_i) + \vec{R}_{QL}, \tag{11}$$

where we now allow the ion temperature T_i to be nonzero and vary spatially. We have introduced the quasilinear force term

$$\vec{R}_{QL} = -e\langle n_1 \nabla\phi_1\rangle, \tag{12}$$

which represents the time-averaged electrostatic force from the fluctuating electric field over a time scale longer than the wave period. We note here that we have neglected ion temperature gradients in the azimuthal direction by the symmetry of the system.

Equation 12 shows that the anomalous force will contribute if the density and potential fluctuations are in-phase to such a degree that the time-average of their product is nonzero. The physical mechanism underlying this force is that the waves, which are primarily carried by ion motion, contribute to variations in the local electric field, which can enhance the average ion drift speed. The energy of the waves, on the other hand, stems from the electron drift. This term thus represents a physical transfer of electron momentum to ion momentum, mediated by the instability.

For the ion temperature, we take the second moment to obtain an effective energy conservation equation. Assuming an adiabatic system, this yields

$$\frac{1}{2}m_i n_0 \frac{du_{i0}^2}{dt} + \frac{3}{2}e\frac{\partial\left(n_0 T_i\right)}{\partial t} + \frac{5}{2}e\left[\vec{u}_{i0}\cdot\nabla\left(n_0 T_i\right) + n_0 T_i \nabla\cdot\vec{u}_{i0}\right] = -\frac{1}{2}e\int v_\theta^2 \left\langle E_1 \frac{\partial f_1}{\partial v_\theta}\right\rangle dv_\theta. \tag{13}$$

The momentum equation (Eq. 11) allows us to eliminate the first term, resulting in the temperature evolution equation

$$\frac{3}{2}\left[\frac{\partial\left(n_0 T_i\right)}{\partial t} + \vec{u}_{i0}\cdot\nabla\left(n_0 T_i\right)\right] + \frac{5}{2}n_0 T_i \nabla\cdot\vec{u}_{i0} = -n_0\langle\vec{u}_{i1}\cdot\nabla\phi_1\rangle. \tag{14}$$

The right hand side of Eq. 14 represents the effect of the oscillating potential and velocity on the variance of the distribution. This effective "heating" term stems from correlations between the electric field fluctuations and the perturbed distribution function, and the magnitude of this heating is dependent on the phase delay between oscillations in these quantities. In principle, if the electric field, density, and average velocity on the time-scales of the waves can be resolved, this offers a prescription for estimating the effective increase in ion temperature based on the local wave amplitudes.

We now assume the plasma is steady and pick out the azimuthal component of the motion, along which the background electric field vanishes. Combined with the condition that the ion velocity is primarily directed axially, this yields

$$u_{iz}\frac{\partial u_{i\theta}}{\partial z} = -\frac{e\langle n_1 \nabla_\theta \phi_1\rangle}{m_i n_0}. \tag{15}$$

We have neglected the ion pressure force here, due to the relatively low ion temperature. Assuming that ions exit the cathode with negligible azimuthal velocity, we can approximate the spatial gradient as $\partial u_{i\theta}/\partial z \approx u_{i\theta}/z$, where z is the axial distance traveled. This allows us to estimate the azimuthal velocity attained by ions streaming axially out of the cathode as

$$u_{i\theta} \approx -\frac{ez}{m_i n_0 u_{iz}}\langle n_1 \nabla_\theta \phi_1\rangle. \tag{16}$$

In cylindrical coordinates, the potential gradient is approximately given by

$$\nabla_\theta \tilde{\phi}_1 \approx \Re\left[i\frac{m}{r}\tilde{\phi}_1\right], \tag{17}$$

which can be related to the density fluctuation via Eq. 4. Thus, the azimuthal swirl speed can be written as

$$u_{i\theta} \approx -\frac{zeT_e}{2m_i u_{i0z}}\frac{m}{r}\Re\left[iK\left|\frac{\tilde{n}_1}{n_0}\right|^2\right]. \tag{18}$$

In order to predict the time-averaged ion temperature in the cathode plume, we assume the temperature profile is steady-state and only consider convection from ion velocity in the axial direction. We also assume that the $\nabla\cdot\vec{u}_{i0}$ term is small and retain only the azimuthal component of the wavevector, resulting in the expression

$$\frac{3}{2}n_0 u_{i0z}\frac{\partial T_i}{\partial z} = -in_0\left(\frac{m}{r}\right)\left\langle u_{i1\theta}\phi_1\right\rangle. \tag{19}$$

In an analogous manner to the drift velocity calculation, we assume ions are cold immediately after exiting the cathode, and approximate the axial temperature growth as linear with z. Along with Eqs. 4 and 5, we obtain the approximate relation

$$T_i \approx -\frac{eT_e^2}{3m_i u_{i0z}}\left(\frac{m}{r}\right)^2\Re\left[\frac{i}{\omega_r - i\gamma - k_z u_{i0z}}|K|^2\left|\frac{\tilde{n}_1}{n_0}\right|^2\right]. \tag{20}$$

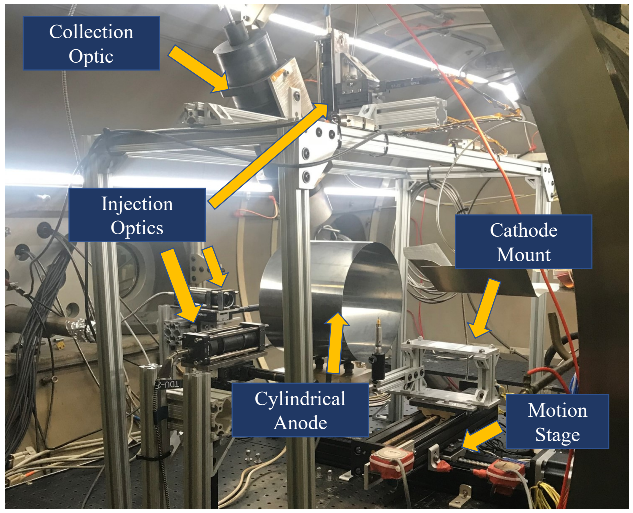

Fig. 2 Photograph of the vacuum chamber with LIF injection optics for testing of the HERMeS hollow cathode.

Equation 20 predicts the ion temperature to quadratic quasilinear order as a function of radial and axial position. Note that as with the drift velocity estimation, the only mechanism for temperature variation considered here is the convective effect of the axial ion drift balanced by the anomalous heating term from the wave fields. While a complete treatment would integrate these governing equations over the full 3D expansion of the cathode plume ions, the current technique is appropriate for estimation of ion temperature variation to be compared with point 1D velocity distribution measurements.

III. Methods

A. Cathode LIF Experiment

In order to directly evaluate the role of rotational cathode waves in producing high ion energies near the cathode, we performed laser-induced fluorescence (LIF) measurements of the ion velocities in the azimuthal direction. LIF is an optical diagnostic technique for particle velocimetry. The technique uses a tunable laser to excite a metastable transition in plasma ions, which decay spontaneously and emit fluorescence. Because of the Doppler shift of the incoming laser photons, the beam excites ions moving at different velocities along the laser axis. Tuning the laser through a range of wavelengths while monitoring the collected fluorescent light intensity provides a proxy for the proportion of ions moving at each speed, allowing for estimation of the ion velocity distribution function (IVDF).

The low signal-to-noise ratio (SNR) typical of LIF measurements is remedied with optical chopping and phase-sensitive detection (PSD). However, the time constant of the requisite lock-in amplification step involves an effective average over long times compared to fast plasma oscillations, destroying time resolution. We achieve high time-resolution with the average transfer function approach of Durot [23]. This technique assumes the linear time-invariant relationship

$$f(\omega) = H(\omega)I(\omega) \tag{21}$$

to link a reference signal $I(\omega)$, such as the discharge current, with the buried LIF signal, $f(\omega)$, in the frequency domain. This allows for synthesis of denoised, time-resolved IVDFs by computing the average transfer function $\langle H(\omega)\rangle$ over a large number of oscillation periods.

We carried out this experiment in a 1.4-meter diameter by 2-meter long vacuum chamber equipped with cryogenic condensation pumps at the Jet Propulsion Laboratory. A photograph of this setup is shown in Fig. 2. The plasma source was the 25-A class hollow cathode developed for the 12-kW Hall Effect Rocket with Magnetic Shielding (HERMeS), built at NASA GRC [24]. We operated the cathode with a 25.4-cm diameter cylindrical anode, displaced 6.8 cm axially from the cathode exit. The anode was composed of a thin rolled molybdenum sheet. Magnetic coils simulated the field shape to mimic Hall thruster operation. The cathode operated at that thruster's nominal discharge current of 20.8 A and at 75% of the nominal AEPS magnetic field strength, measured on channel centerline. Laser light was focused to a sub-mm interrogation spot along the azimuthal direction from above the cathode, and two-axis motion stages enabled horizontal translation along the cathode center plane. Figure 3 displays a schematic of the test setup.

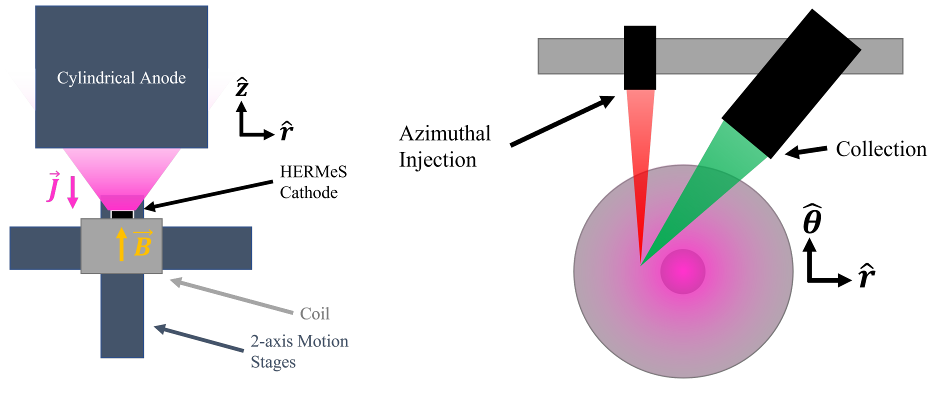

(a) **(b)**

Fig. 3 Schematic of the AEPS cathode apparatus used for the experiment. a) Top-down view of the apparatus. b) front view of the LIF injection and collection optics.

We used a tunable diode laser to target the xenon I metastable transition at 834.953 nm in vacuum. We modulated the laser power with an acousto optic modulator (AOM), then fiber-coupled the modulated beam to a positive lens with 50-mm focal length which focused the light to the interrogation zone. Fluorescent light at a wavelength of 541.2 nm entered another optic which imaged the interrogation spot. An optical fiber carried this light to a spectrally-filtered photomultiplier tube (PMT). In the case of time-averaged measurements, the PMT signal was converted to voltage with a trans-impedance amplifier. This signal as well as the 3-kHz modulation waveform input into an SRS-830 lock-in amplifier for PSD. For time-resolved measurements, we modulated the laser at a higher frequency of 1.8 MHz. We then terminated the PMT with a 1-kΩ resistor for fast response and PSD was carried out programmatically in post-processing. Further details of the transfer-function time-resolved LIF apparatus are contained in Ref. 25.

We first took a spatial profile of the time-averaged ion properties, followed by time-resolved measurements at the denoted points where wave amplitudes were expected to be large. The fact that all measurements were taken on the horizontal center plane of the cathode allow the definition of a 2D coordinate system with the origin on centerline at cathode exit. Radial positions are defined as positive on the right of cathode centerline, looking down from above the plasma source. All dimensions are normalized to the cathode keeper radius, denoted R_{keep}.

B. Data Analysis

Each local LIF trace yields relative intensity values as a function of laser wavelength. Wavelength is converted to ion velocity based on Doppler scaling. Figure 4 shows a typical ion velocity distribution in the azimuthal direction. Average fluid properties of the ion species can be defined as kinetic moments of the velocity distribution. The mean velocity is computed as the normalized first moment, while the effective temperature is defined as the variance of the distribution in units of energy. This kinetic definition of temperature is valid even for small deviations from equilibrium, for example when there is a "tail" of high energy ions. In this paper, the terms "temperature" and "heating" refer to this spread in kinetic energies along the interrogation direction, and do not imply equilibrium or even isotropy.

We used an analytical curve-fitting scheme to approximate the measured IVDFs as sums of Gaussian distributions. The general model is of the form

$$f(v) = c_1 \exp \frac{(v - c_2)^2}{c_3^2} + c_4 \exp \frac{(v - c_5)^2}{c_6^2}. \tag{22}$$

Simpler equilibrium distributions can be adequately fit with only the first term in the sum ($c_4 = 0$), but the second peak allows for the fitting of small non-equilibrium features in the wings of more complex distributions. Note that this fitting model does not imply two separate populations of ions; in this work, all of the measured IVDFs displayed a single main population, often with small non-Maxwellian features.

To estimate uncertainty, we implemented a Markov-Chain Monte Carlo (MCMC) algorithm to sample from a posterior distribution of likely curve fits based on Bayes' Theorem. The curves overlaid on the data in Fig. 4 are

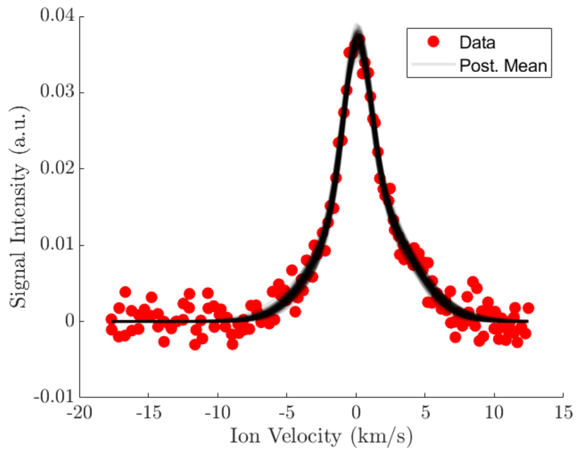

Fig. 4 Example time-averaged azimuthal IVDF (red data) with overlaid curves from the MCMC fit distribution.

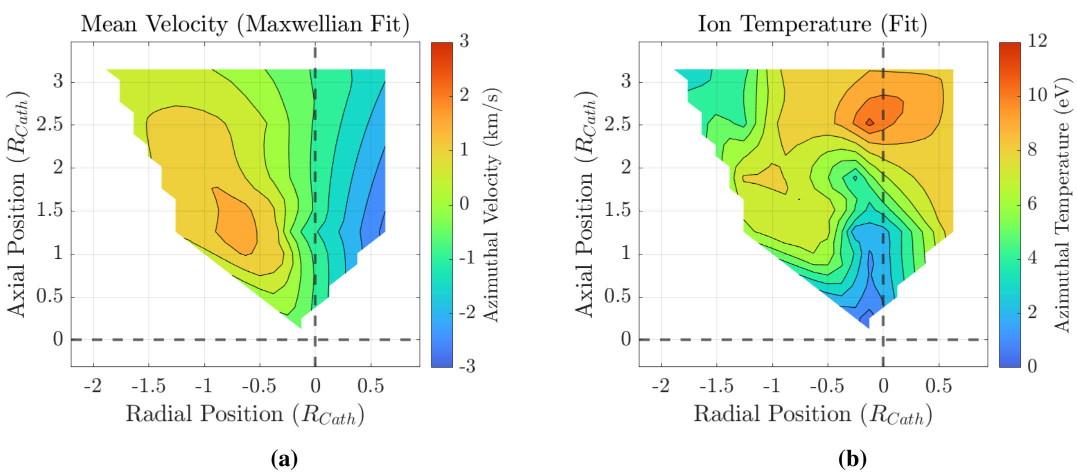

Fig. 5 Time-averaged mean azimuthal ion velocities (a) and temperatures (b) near the cathode exit.

examples of these likely curve fits, where the width of their values at a given velocity demonstrates the uncertainty in the fit there. These samples of curve fit parameters can be processed to propagate the uncertainty to final fluid property values. We instead used a faster, least-squares/frequentist fitting algorithm for the time-resolved IVDFs, due to the large volume of data.

IV. Results

A. Time-Averaged Ion Properties

We first focus on the results of the time-averaged LIF measurements. Figure 5a displays a contour plot of the mean azimuthal ion velocities over the spatial measurement domain. We obtained these mean velocities with the fitting algorithm described in Section III.B. The ion population exhibits a swirling motion: azimuthal velocities are directed upward for negative radial coordinates, whereas at positive radial positions the ions move downward. The ions acquire a maximum swirl velocity of nearly 2 km/s in a localized region downstream of the exit plane. Azimuthal velocities are nearly zero on cathode centerline, corresponding to the plume's cylindrical symmetry.

Ions exiting the cathode initially display low temperatures below 1 eV, as shown in Fig. 5b. However, the ions gain a larger spread in azimuthal kinetic energy as they expand outward from the cathode. The temperature reaches a local maximum of 6-8 eV in the same region in which the swirl speed is maximized. Downstream heating is also

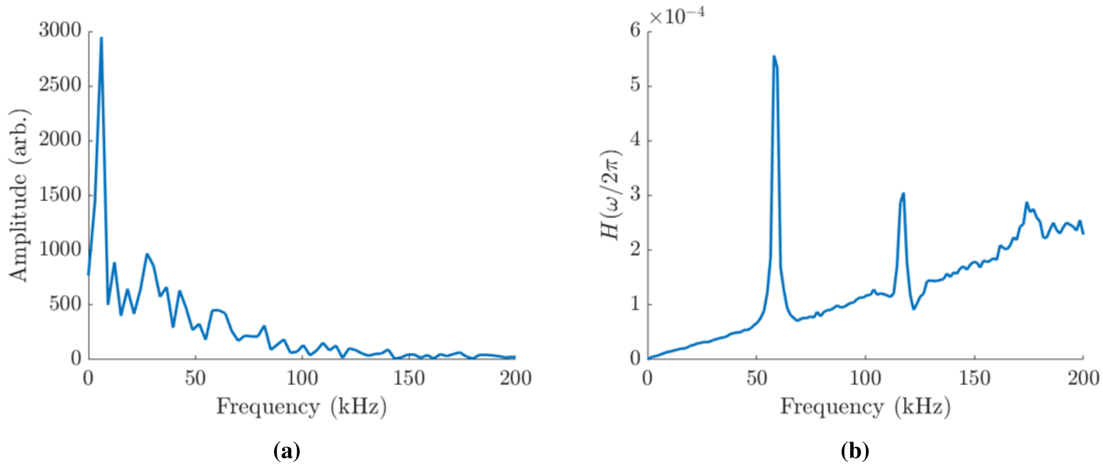

Fig. 6 Frequency-domain analysis for transfer-function time-resolved LIF: (a) Fourier transform of the discharge current reference signal (b) Estimated transfer function for a wavelength in the center of the time-averaged IVDF.

evident on channel centerline, up to even higher temperatures of 12 eV. The location of accelerated and heated ions is consistent with the localized, off-axis region of large wave activity measured in the H9 thruster in Ref. 17. However, direct measurement of the time-resolved response of the ion distribution is necessary to definitively link these azimuthal properties with cathode wave behavior.

B. Time-Resolved Ion Properties

We used the cathode discharge current as the reference signal for the transfer-function LIF analysis. The Fourier spectrum of a representative discharge current trace is shown in Fig. 6a. A low-frequency spike near 10 kHz is apparent, and the content gradually decays with higher frequencies. Notably, no large spike is evident at the 60-kHz frequency corresponding to the cathode waves. Figure 6b displays the estimated average transfer function computed from the reference signal for a particular wavelength. Despite the lack of prominent frequency-domain structure in the reference signal, the transfer function has large spikes corresponding to the fundamental, 60-kHz mode of the wave as well as its harmonics. This demonstrates that while it is not immediately apparent that the discharge current contains information corresponding with the azimuthal oscillations, averaging the complex phase and amplitude information for a long acquisition enables this technique to synthesize physically real behavior of the LIF signal from correlations with the discharge current.

Figure 7 demonstrates the time-resolved azimuthal IVDFs at two locations in the plume. At each time, the IVDF is renormalized to its own maximum, which allows discernment of the entire IVDF shape without reference to fluctuations in the total light intensity. The ions oscillate periodically in velocity-space at 60 kHz, the same frequency as the fundamental mode found in the transfer function. This oscillation displays a nearly sinusoidal waveform; however, there is a slight asymmetry. Ions rapidly speed up to a higher range of velocities between 2-5 km/s, then gradually ramp down to a range between -2 and 1 km/s each cycle. The longer time window in Fig. 7b demonstrates that the wave structure sometimes shifts from a more chaotic ion oscillation to coherent, nearly-sinusoidal oscillations.

Figure 8 shows the time-resolved mean velocity, intensity, and temperature in the same location as Fig. 7a. The mean velocity parameterizes the shift in the center of the IVDF with time. In addition to the center velocity, the total light intensity was also found to oscillate strongly at the wave frequency. Since the collected LIF signal is proportional to the number of ions excited by the beam, this fluctuating light intensity can be used as a proxy for the plasma density oscillations within the interrogation volume, under the assumption that the electron temperature (and therefore the proportion of ions which occupy the metastable state targeted by LIF) is constant. The instantaneous intensity plotted in Fig. 8a is calculated as the total area under the curve of the non-normalized IVDF, and is related to the fractional density fluctuation. The mean velocity and density oscillate nearly in phase at the wave frequency, with the peaks and troughs of the density oscillation lagging slightly behind.

The mean velocity moves consistently with this sloshing of the IVDF observed in Fig. 7. The ion temperature, however, exhibits no strong oscillations at the wave frequency. There are occasional spikes in ion temperature upwards

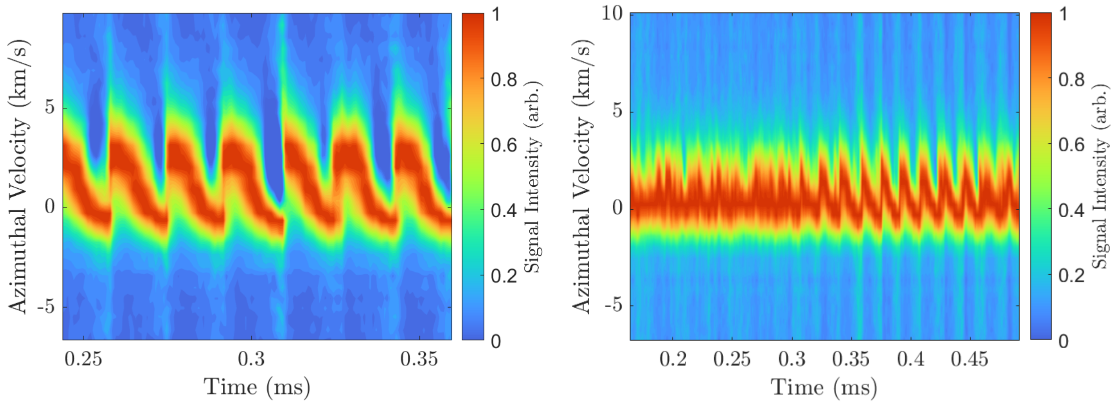

(a) **(b)**

Fig. 7 Time-resolved azimuthal ion velocity distribution in the presence of 60-kHz cathode waves, at (r, z) positions $(-1.3, 1.3) \cdot R_{Keep}$ and $(-1.9, 1.3) \cdot R_{Keep}$, respectively.

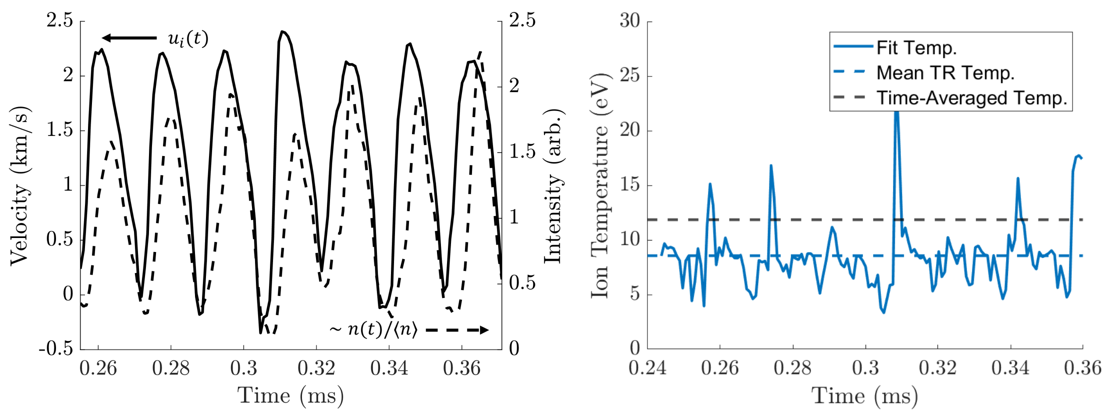

(a) **(b)**

Fig. 8 Time-resolved mean velocity and intensity (a), and temperature (b) at the position of maximum oscillation amplitude.

of 12-20 eV; these rapid increases coincide with oscillation phases during which the ions are shifting from low to high velocity. Rather than interpret these large instantaneous ion temperatures as physical, it is likely that due to bandwidth limitations of the diagnostic, the rapid shift in the distribution is averaged over. This would contribute an apparent broadening during these shifts, consistent with the temperature profile seen in Fig. 8b.

The amplitude of these fluctuations varies with location. Figure 9 displays a spatial map of the peak-to-peak ion oscillation amplitude. These values are calculated by taking the difference between the maximum and minimum time-resolved mean ion velocities achieved over several wave periods in each location. The oscillation strength displays a correlation with the magnitude of the time-averaged properties, with the peak-to-peak amplitude maximized in the same region as the time-averaged swirl speed and temperature. This is consistent with probe measurements of the amplitudes of these waves in the similar H9 Hall thruster, which displayed a localized region of peaked amplitudes off-axis [17]. The maximum peak-to-peak amplitudes are on the order of 6 km/s.

V. Discussion

In this section, we compare the properties of the ion distribution as well as its first two moments to the behavior predicted by quasilinear theory in Section II.

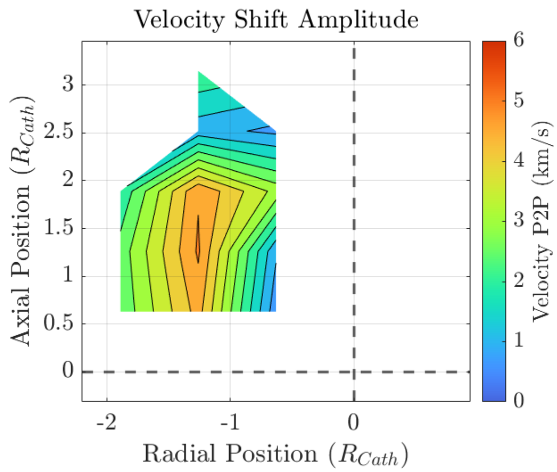

Fig. 9 Spatial variation of the amplitude of ion velocity oscillations in the azimuthal direction.

A. Impact of Waves on Ion Distribution

Figure 10a displays the results of applying the theoretical framework developed in section II to evaluate the perturbation of the $m = 1$ mode to the distribution function. To generate this plot, we numerically evaluated a fit to the time-averaged LIF trace in the location of maximum-amplitude velocity oscillations. We then applied numerical differentiation and solved the dispersion relation in Eq. 2 for the growth rate to evaluate $f_1(v_\theta, t)$, given by Eq. 9. This perturbation was added to the original time-resolved fit to obtain the total distribution function plotted here. For the purposes of this calculation, we assumed the drift speeds and ambient plasma properties to be commensurate with probe measurements from the H9 thruster in Ref. 17. The real part of the frequency is taken from the oscillations in the LIF data as opposed to this analytical calculation for ease of comparison. Figure 10b shows a contour of the time-resolved fits to the LIF data in the corresponding location. Both contours are normalized to the maximum height of the IVDF at each time step.

The experimental IVDF agrees well with the time-resolved distribution function predicted by linear wave theory. A similar sloshing of $f(v)$ between low and high average velocities is observed in both cases, ranging from roughly -1 to 5 km/s from minimum to maximum. This can be understood through the fact that the time-averaged distribution is nearly Maxwellian; since $\partial f_0/\partial v_\theta$ is an odd function about its mean velocity, the perturbation predicted by Eq. 9 vibrates back and forth with the oscillating electric field. Despite this encouraging agreement, a few discrepancies are noted. Firstly, the experimental IVDF oscillations are asymmetrical when contrasted with the sinusoidal waveform of the predicted oscillation. The experimental IVDF experiences a much shorter rise time to shift to a higher velocity, compared to the time it takes to fall back to a lower velocity. The instantaneous width of the distribution is also more narrow in the data, suggesting a more complex velocity dependence for the perturbation amplitude. These discrepancies are likely due to the combined result of neglecting higher harmonics in the model as well as nonlinear wave behavior due to the large amplitude of the oscillations.

B. Impact of Waves on Average Ion Swirl

The time-resolved measurements depict an IVDF with relatively constant temperature shifting back and forth in mean velocity as the wave passes by in the azimuthal direction. The time-average of this shifting IVDF has a nonzero mean velocity. This elevated velocity is caused by an acceleration over time scales longer than the wave period, and can be understood in terms of the quasilinear collision term acting on the ion distribution, as described in Section II.

Figure 11a shows the time-averaged mean velocity from the LIF data in addition to the predictions from the linear theory. Both measurements and calculations are performed for multiple radial locations at a downstream axial position of 1.3 keeper radii. For the theory values, we evaluate Eq. 18 to estimate the ion velocity produced by time-averaged wave acceleration based on the local plasma properties. Due to the lack of in-situ probe measurements during this experiment, we use the representative values $T_e \approx 5$ eV, $u_{i0z} \approx 1$ km/s, and $\nu_e \approx 10^7$ Hz, again obtained from Langmuir probe measurements near the H9 thruster cathode in Ref. 17. The drift speeds and other local plasma parameters are denoted in Table 1 of that reference. For the amplitude of the density fluctuation n_1/n_0, we use the time-resolved total

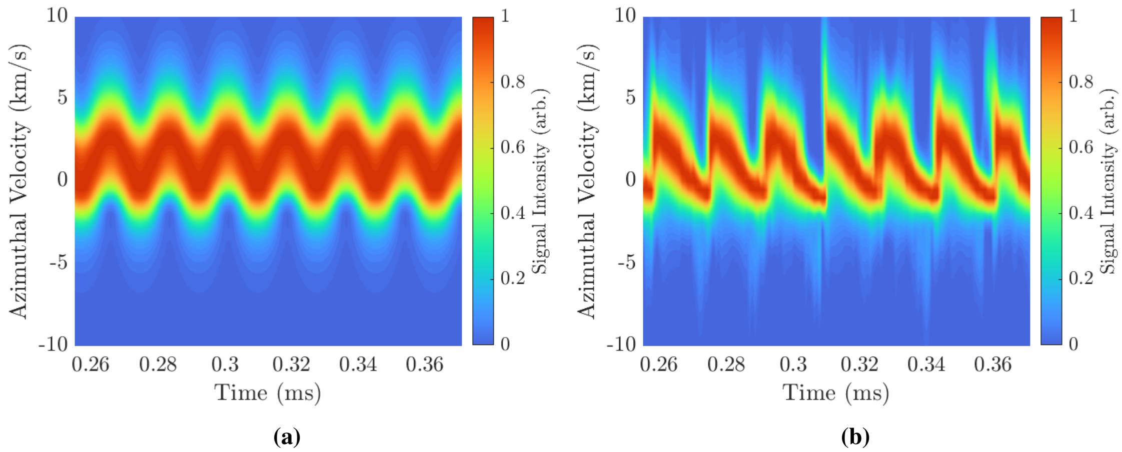

Fig. 10 Theoretical and experimental oscillations in the ion velocity distribution. a) Predicted IVDF oscillation calculated from Eq. 9. b) Contour plot of fits of the time-resolved experimental data.

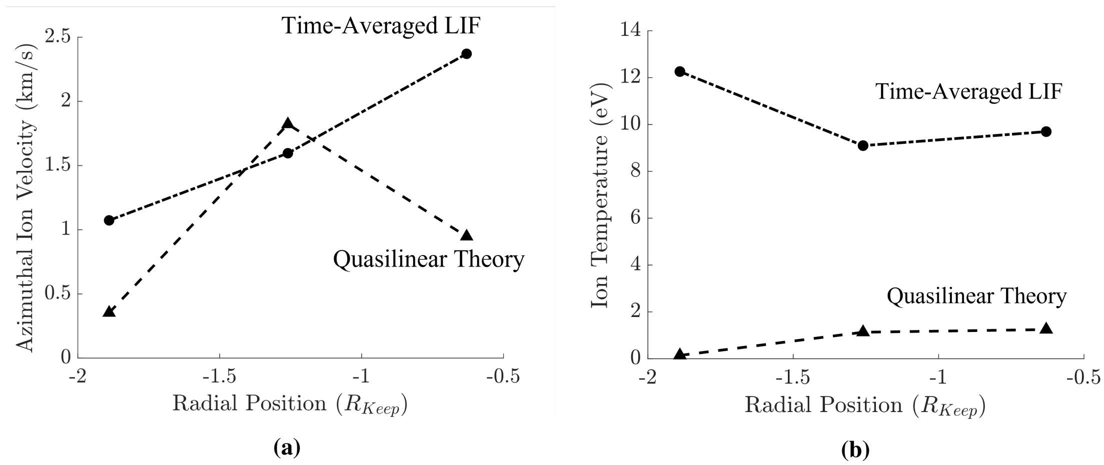

Fig. 11 Theoretical and experimental moments of the ion velocity distribution. a) Mean azimuthal ion velocity. b) Azimuthal ion temperature.

fluorescent light intensity collected by the LIF optic as a local measure (See Fig. 8a). This assumption is enabled by the fact that the total fluorescent light should be proportional to the density of ions within the interrogation volume. However, it must be noted that corresponding fluctuations in electron temperature, which mediate the proportion of ions found in the metastable state targeted by LIF, may corrupt this result. Despite this, in the current work we take the total light intensity to be a representative measure of the relative amplitude of density fluctuations in the plasma.

The order of magnitude of the measured ion velocities agrees with the predictions, although the experimental values differ by up to a factor of 3 in some locations. This demonstrates that even with our limited framework for estimating the ion velocities, the energies observed in the azimuthal direction are consistent with those that can be supplied by the wave fields. Discrepancies can arise based on the fact that we have neglected radial ion motion, which can contribute to convection of increased ion energies as the cathode plume expands. Additionally, the possibility exists that the simple linear framework for wave acceleration fails to capture the complete ion dynamics due to nonlinear wave growth. If so, direct measurements of the oscillating plasma potential, for example with emissive probes, would enable a direct comparison between the ion velocities and the wave acceleration field allowing for nonlinear behavior. Finally, the precise scaling of the wave-induced velocity with radius may be altered by the quasi-Cartesian wavenumber $k_\theta \sim \frac{m}{r}$, which is a local approximation for a more complete global model in cylindrical coordinates.

C. Impact of Waves on average ion temperature

Figure 11b compares the breadth of the experimental distributions to predictions of ion temperature based on the quasilinear heating mechanism described in Section II at an axial distance of 1.3 R_{keep}. In the same manner to the mean velocities, we estimated the downstream ion temperature by evaluating Eq. 20 with local equilibrium plasma properties from measurements in the H9 [17] and inferring the normalized wave amplitude from the LIF fluorescent intensity oscillations. The measured ion temperatures are higher than the predicted values by nearly an order of magnitude, which suggests that this quasilinear approach does not fully capture the dynamics leading to the high ion temperatures observed in this region.

As with the other metrics for comparison, differences between the observed profiles and the predictions from theory likely stem from assumptions made in the simple derivation presented in Section II. The neglect of radial convection processes in the ion energy equation, as well as the potential nonlinearity of the waves in question, could lead to underpredictions of the ion energies. In particular, our formulation for temperature depends quadratically on the amplitude of oscillations in the electrostatic potential; if ϕ_1 in fact depends on n_1/n_0 in a more complicated manner than the linear scaling predicted here, this could significantly increase the ion heating experienced near the keeper and poles. It is also possible that an additional heating mechanism is present which is not captured by the LIF diagnostic, for example anomalous heating by wave processes faster than this approach's ~100 kHz bandwidth limit.

Despite the disagreement in exact values, the conclusion remains that the large azimuthal ion temperatures observed in the cathode plume are highly spatially correlated with the amplitude of the ion oscillations (Fig. 5b and 9). This suggests that whether by the mechanism presented here or by a more complex or nonlinear effect, energy transfer from the anti-drift wave to ions in the cathode plume can increase ion temperatures to large values. The increased temperatures and velocities observed in this region may in turn increase the flux of energetic ions at oblique angles of incidence to the pole and keeper surfaces in a Hall thruster, thereby elevating erosion rates.

VI. Conclusion

We performed time-resolved LIF measurements in a hollow cathode plume with a simulated Hall thruster magnetic field to evaluate the ion properties in the azimuthal direction. The azimuthal ion velocity distribution oscillates strongly at the frequency of the cathode waves, consistent with a quasilinear description of the ion population responding to an azimuthal anti-drift mode. Time-averaged LIF revealed increased ion velocities and temperatures along the azimuthal direction. Ions swirl azimuthally at time-averaged mean velocities of up to 2 km/s near the keeper face, and temperatures range from below 1 eV at the cathode exit to 8-12 eV slightly downstream. The magnitudes of these increases are correlated with the locations at which the amplitude of ion oscillations is maximized, suggesting that wave effects could lead to the observed acceleration and heating of the ion population. Simple kinetic calculations can accurately describe the qualitative characteristics of the oscillation as well as the order of magnitude of the mean velocities, but this framework underpredicts ion temperatures by nearly an order of magnitude and does not fully capture scaling with radial distance. This suggests that while the anti-drift waves are able to measurably exchange energy with the ions in the near-field cathode plume, further analysis is required to fully explain the exact nature of wave-particle energy exchange and large ion temperatures in this region.

Acknowledgments

The research was carried out at the Jet Propulsion Laboratory, California Institute of Technology, under a contract with the National Aeronautics and Space Administration (80NM0018D0004). The work was sponsored by a NASA Space Technology Graduate Research Opportunity. Thanks is extended to Dr. Jay Polk, Dr. Alejandro Lopez Ortega, and Dr. Ioannis Mikellides for aid in experimental setup as well as helpful discussion. Additionally, the authors thank Nowell Niblett for help in constructing the test apparatus.

References

[1] Yim, J. T., "Computational Modeling of Hall Thruster Channel Wall Erosion," Ph.D. thesis, University of Michigan, 2008. URL `http://deepblue.lib.umich.edu/bitstream/2027.42/58446/1/johnyim_1.pdf`.

[2] Peterson, P. Y., and Manzella, D. H., "Inverstigation of the Erosion Characteristics of a Laboratory Hall Thruster," *39th AIAA/ASME/SAE/ASEE Joint Propulsion Conference and Exhibit*, Huntsville, Alabama, 2003, pp. 1–9. https://doi.org/10.2514/6.2003-5005.

[3] Mikellides, I. G., Katz, I., Hofer, R. R., and Goebel, D. M., "Magnetic shielding of a laboratory Hall thruster. I. Theory and validation," *Journal of Applied Physics*, Vol. 115, No. 4, 2014, p. 043303. https://doi.org/10.1063/1.4862313, URL http://aip.scitation.org/doi/10.1063/1.4862313.

[4] Hofer, R. R., Goebel, D. M., Mikellides, I. G., and Katz, I., "Magnetic shielding of a laboratory Hall thruster. II. Experiments," *Journal of Applied Physics*, Vol. 115, No. 4, 2014, p. 043304. https://doi.org/10.1063/1.4862314, URL http://aip.scitation.org/doi/10.1063/1.4862314.

[5] Sekerak, M. J., Hofer, R. R., Polk, J. E., Jorns, B. A., and Mikellides, I. G., "Wear Testing of a Magnetically Shielded Hall Thruster at 2000 s Specific Impulse," *34th International Electric Propulsion Conference*, Hyogo-Kobe, Japan, 2015, pp. 1–37.

[6] Frieman, J. D., Gilland, J. H., Kamhawi, H., Mackey, J., Williams, G. J., Hofer, R. R., and Peterson, P. Y., "Wear trends of the 12.5 kW HERMeS Hall thruster," *Journal of Applied Physics*, Vol. 130, No. 14, 2021, p. 143303. https://doi.org/10.1063/5.0062579, URL https://doi.org/10.1063/5.0062579https://aip.scitation.org/doi/10.1063/5.0062579.

[7] Lopez Ortega, A., Mikellides, I. G., and Katz, I., "Hall2De numerical simulations for the assessment of pole erosion in a magnetically shielded Hall thruster," *34th International Electric Propulsion Conference*, Hyogo-Kobe, Japan, 2015, pp. IEPC–2015–249.

[8] Lopez Ortega, A., Mikellides, I. G., Sekerak, M. J., and Jorns, B. A., "Plasma simulations in 2-D (r-z) geometry for the assessment of pole erosion in a magnetically shielded Hall thruster," *Journal of Applied Physics*, Vol. 125, No. 3, 2019, p. 033302. https://doi.org/10.1063/1.5077097, URL http://dx.doi.org/10.1063/1.5077097.

[9] Lopez Ortega, A., and Mikellides, I. G., "Investigations of Pole Erosion Mechanisms in the 12.5 kW HERMeS Hall Thruster Using Numerical Simulations and Ion Velocity Measurements," *AIAA Propulsion and Energy Forum*, 2018 Joint Propulsion Conference, Cincinnati, Ohio, 2018, pp. AIAA 2018–4647. https://doi.org/10.2514/6.2018-4647.

[10] Lopez Ortega, A., Mikellides, I. G., and Chaplin, V. H., "Numerical Simulations for the Assessment of Erosion in the 12.5-kW Hall Effect Rocket with Magnetic Shielding (HERMeS)," *35th International Electric Propulsion Conference*, Atlanta, Georgia, 2017, pp. IEPC–2017–154. URL https://iepc2017.org/sites/default/files/speaker-papers/iepc-2017-154_final_postdocrev.pdf%0Ahttp://erps.spacegrant.org/IEPC_2017/IEPC_2017_154.pdf.

[11] Jorns, B. A., Dodson, C., Anderson, J., Goebel, D. M., Hofer, R. R., Sekerak, M., Lopez Ortega, A., and Mikellides, I., "Mechanisms for Pole Piece Erosion in a 6-kW Magnetically-Shielded Hall Thruster," *Propulsion and Energy Forum*, 52nd AIAA/SAE/ASEE Joint Propulsion Conference, Salt Lake City, Utah, 2016, pp. AIAA 2016–4839. https://doi.org/10.2514/6.2016-4839.

[12] Huang, W., and Kamhawi, H., "Counterstreaming ions at the inner pole of a magnetically shielded Hall thruster," *Journal of Applied Physics*, Vol. 129, No. 04, 2021, p. 043305. https://doi.org/10.1063/5.0029428, URL https://doi.org/10.1063/5.0029428.

[13] Mikellides, I. G., and Lopez Ortega, A., "Growth of the lower hybrid drift instability in the plume of a magnetically shielded Hall thruster," *Journal of Applied Physics*, Vol. 129, No. 19, 2021, p. 193301. https://doi.org/10.1063/5.0048706, URL https://aip.scitation.org/doi/10.1063/5.0048706.

[14] Mikellides, I. G., and Lopez Ortega, A., "Growth of the modified two-stream instability in the plume of a magnetically shielded Hall thruster," *Physics of Plasmas*, Vol. 27, No. 10, 2020, p. 100701. https://doi.org/10.1063/5.0020075, URL http://aip.scitation.org/doi/10.1063/5.0020075.

[15] Lopez Ortega, A., Mikellides, I. G., Chaplin, V. H., Huang, W., and Frieman, J. D., "Anomalous Ion Heating and Pole Erosion in the 12.5-kW Hall Effect Rocket with Magnetic Shielding (HERMeS)," *AIAA Propulsion and Energy 2020 Forum*, American Institute of Aeronautics and Astronautics, Reston, Virginia, 2020, pp. AIAA 2020–3620. https://doi.org/10.2514/6.2020-3620, URL https://arc.aiaa.org/doi/10.2514/6.2020-3620.

[16] Jorns, B. A., and Hofer, R. R., "Plasma oscillations in a 6-kW magnetically shielded Hall thruster," *Physics of Plasmas*, Vol. 21, No. 5, 2014, p. 053512. https://doi.org/10.1063/1.4879819, URL http://dx.doi.org/10.1063/1.4879819http://aip.scitation.org/doi/10.1063/1.4879819.

[17] Jorns, B. A., Cusson, S. E., Brown, Z., and Dale, E., "Non-classical electron transport in the cathode plume of a Hall effect thruster," *Physics of Plasmas*, Vol. 27, No. 2, 2020, p. 022311. https://doi.org/10.1063/1.5130680, URL http://aip.scitation.org/doi/10.1063/1.5130680.

[18] Hepner, S. T., Tang, E., Dale, E. T., and Jorns, B. A., "Rotational Waves in the Plume of an Externally-Mounted Hall Thruster Cathode," *AIAA Journal*, 2021, pp. 1–5. https://doi.org/10.2514/1.J060578, URL https://arc.aiaa.org/doi/10.2514/1.J060578.

[19] Huang, W., Kamhawi, H., and Haag, T., "Plasma Oscillation Characterization of NASA's HERMeS Hall Thruster via High Speed Imaging," *52nd AIAA/SAE/ASEE Joint Propulsion Conference*, American Institute of Aeronautics and Astronautics, Reston, Virginia, 2016, pp. AIAA–2016–4829. https://doi.org/10.2514/6.2016-4829, URL http://arc.aiaa.org/doi/10.2514/6.2016-4829.

[20] Jorns, B. A., and Byrne, M. P., "Model for the dependence of cathode voltage in a Hall thruster on facility pressure," *Plasma Sources Science and Technology*, Vol. 30, No. 1, 2021, p. 015012. https://doi.org/10.1088/1361-6595/abd3b6, URL https://iopscience.iop.org/article/10.1088/1361-6595/abd3b6.

[21] Ellis, R. F., Marden-Marshall, E., and Majeski, R., "Collisional drift instability of a weakly ionized argon plasma," *Plasma Physics*, Vol. 22, No. 2, 1980, pp. 113–131. https://doi.org/10.1088/0032-1028/22/2/002, URL https://iopscience.iop.org/article/10.1088/0032-1028/22/2/002.

[22] Frias, W., Smolyakov, A. I., Kaganovich, I. D., and Raitses, Y., "Long wavelength gradient drift instability in Hall plasma devices. II. Applications," *Physics of Plasmas*, Vol. 20, No. 5, 2013, p. 052108. https://doi.org/10.1063/1.4804281, URL http://aip.scitation.org/doi/10.1063/1.4804281.

[23] Durot, C. J., "Development of a Time-Resolved Laser-Induced Fluorescence Technique for Nonperiodic Oscillations," Ph.D. thesis, University of Michigan, 2016.

[24] Hall, S. J., Gray, T. G., Yim, J. T., Choi, M., Mooney, M. M., Sarver-Verhey, T. R., and Kamhawi, H., "The Effect of Anode Position on Operation of a 25-A class Hollow Cathode," *36th International Electric Propulsion Conference*, Vienna, Austria, 2019, pp. IEPC–2019–300. URL https://ntrs.nasa.gov/search.jsp?R=20190032078.

[25] Chaplin, V. H., Lobbia, R. B., Lopez Ortega, A., Mikellides, I. G., Hofer, R. R., Polk, J. E., and Friss, A. J., "Time-resolved ion velocity measurements in a high-power Hall thruster using laser-induced fluorescence with transfer function averaging," *Applied Physics Letters*, Vol. 116, No. 23, 2020, p. 234107. https://doi.org/10.1063/5.0007161, URL http://aip.scitation.org/doi/10.1063/5.0007161.